Intermetallic Pd₃Pb Nanoplates Enhance Oxygen Reduction Catalysis with Excellent Methanol Tolerance

Kai Wang, Yingnan Qin, Fan Lv, Mingqiang Li, Qiao Liu, Fei Lin, Jianrui Feng, Chao Yang, Peng Gao, and Shaojun Guo*

Herein, a new class of intermetallic Pd₃Pb square nanoplates (SNP) and nanoplates assemblies is demonstrated with tunable crystalline orientation for boosting oxygen reduction reaction (ORR) activity and stability with excellent methanol tolerance. The Pd₃Pb intermetallic nanostructures show the crystalline-orientation-dependent electrocatalytic activity for ORR with (100)-facet-dominated Pd₃Pb SNP being the most active. The Pd₃Pb intermetallic SNP exhibits the highest ORR mass activity of 0.78 A mg^{-1} at 0.9 V versus reversible hydrogen electrode in alkaline electrolyte for the state-of-art reported Pd-based nanocatalysts, 7.1 times higher than that of commercial Pt/C. The unique structure of Pd₃Pb intermetallic SNP makes it highly stable for ORR with almost no activity decrease and no composition and morphology changes after a 5000-cycle durability test. The Pd₃Pb intermetallic SNP also exhibits much higher methanol tolerance behavior than commercial Pt/C and Pd/C during ORR catalysis. Density functional theory calculations reveal that presence of Pb decreases adsorption strength of methanol on Pd₃Pb intermetallic SNP. The calculated $E_{methanol}$ follows the order of Pd₃Pb (100) < Pd (111) < Pt (111) with (100)-oriented Pd₃Pb SNP having the lowest methanol adsorption energy, thus boosting methanol tolerance performance.

The proton-exchange-membrane fuel cells (PEMFCs) are being actively pursued to be a leading alternative renewable energy technology to provide power for automotives and portable electronic devices.[1] In PEMFCs, electrocatalysts are the key components in accelerating both reactions of anodic fuel oxidation and cathodic oxygen reduction reaction (ORR).[2] Platinum (Pt) nanoparticles (NPs) supported on carbon black (Pt/C) are the most widely used electrocatalysts for ORR in PEMFCs. However, they usually exhibit sluggish ORR kinetics and limited stability because of the well-known aggregation effect of small NPs.[2b,3] One of the biggest problems for Pt-based ORR catalytic system is related to its limited reserves on earth.[4] Besides, Pt is easily to be poisoned by methanol in PEMFCs as methanol would crossover from anode to cathode through the proton exchange membrane.[5] In this regard, the replacement of scarce Pt metal with more abundant materials, which exhibit excellent methanol tolerance and better ORR catalysis than Pt catalyst, is a critical step in the development of future PEMFCs.

Pd-based bimetallic nanocatalysts have come into sight for ORR due to their obvious advantages of high abundance and low cost.[6] Nevertheless, the biggest challenging issue for the reported Pd-based bimetallic nanocatalysts is their limited activity and stability as they lack the effective electronic or strain effect from the second metal atom to Pd and also rapidly dissolve into the electrolyte during practical fuel cell operation due to their disordered structure.[7] On the contrary, ordered intermetallic structure would provide strong interaction between the second metal and Pd, avoid deactivation, and provide long-term stability.[8] However, the designed synthesis of intermetallic Pd-based intermetallic nanosheets (NS) by taking advantage of the intermetallic structure (guaranteeing stability), high specific surface area, and high fraction of active sites on their surface is still a grand challenge.[9]

Herein, we report our recent achievement in the controlled synthesis of intermetallic Pd₃Pb square nanoplates (SNP) and

K. Wang, Y. Qin, F. Lv, F. Lin, J. Feng, C. Yang, Prof. S. Guo
Department of Materials Science and Engineering
College of Engineering
Peking University
Beijing 100871, China
E-mail: guosj@pku.edu.cn
M. Li, Prof. P. Gao
Electron Microscopy Laboratory, and International Center
for Quantum Materials
School of Physics
Peking University
Beijing 100871, China

Q. Liu
Laboratory of Heat and Mass Transport at Micro-Nano Scale
College of Engineering
Peking University
Beijing 100871, China
Prof. S. Guo
BIC-ESAT
College of Engineering
Peking University
Beijing 100871, China

nanoplates assemblies (NPA) with tunable crystalline orientation for boosting ORR activity and stability with excellent methanol tolerance. We find that the morphology and crystalline orientation of 2D Pd_3Pb nanostructures are closely related to the added amount of $Pb(acac)_2$. With increasing the content of $Pb(acac)_2$, the morphology of Pd_3Pb changed from NPA to SNP with increased (100) facet orientation. The Pd_3Pb SNP with (100) preferred orientation shows higher electrocatalytic activity for ORR than Pd_3Pb NPA with less (100) preferred orientation. The intermetallic Pd_3Pb SNP has high ORR mass activity of 0.78 A mg^{-1} of palladium at 0.9 V versus reversible hydrogen electrode (RHE), 7.1 times higher that of commercial Pt/C. It is also very stable for ORR by showing minor activity decay and no obvious structure and composition changes after a 5000-cycle electrochemical accelerated durability test (ADT). Most importantly, the Pd_3Pb SNP possesses very high methanol tolerance and excellent stability in methanol during electrochemical oxygen reduction process. Density functional theory (DFT) calculations reveal that presence of Pb decreases

adsorption strength of methanol on Pd_3Pb, and the calculated $E_{methanol}$ follows the order of Pd_3Pb (100) < Pd (111) < Pt (111), in which 3d states of Pd_3Pb is closer to Fermi level than those of Pd and Pt. Therefore, Pd_3Pb SNP with (100) preferred orientation have the lowest methanol adsorption energy, thus enhancing methanol tolerant performance.

A wet chemical method was used to make Pd_3Pb SNP using $Pd(acac)_2$ and $Pb(acac)_2$ as metal precursors, ascorbic acid (AA) as reductant, oleylamine (OAm) and 1-octadecene (ODE) as mixed solvents and surfactants, and NH_4Br as structure-directing agent. The morphology and structure of Pd_3Pb square nanoplates were characterized using transmission electron microscopy (TEM), high-resolution transmission electron microscopy (HRTEM), selected-area electron diffraction (SAED), energy-dispersive X-ray (EDX), X-ray photoelectron spectroscopy (XPS), and atomic force microscopy (AFM). TEM images (**Figure 1**a,b) reveal that square nanoplates with an edge length of ≈200 nm are the dominant products. HRTEM (Figure 1c) and SAED (Figure 1d) images show that the Pd_3Pb square nanoplates are highly crystalline
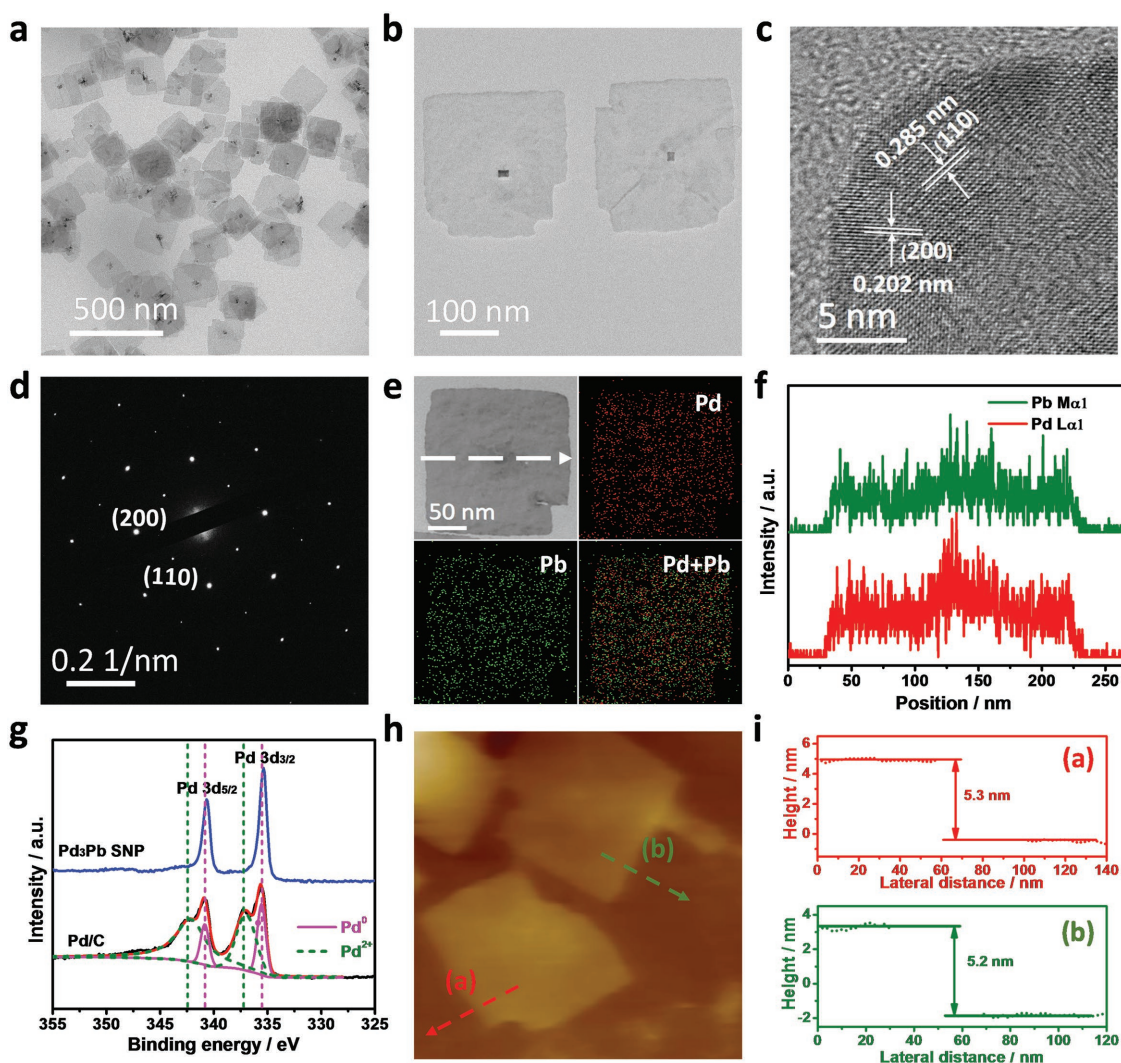

Figure 1. Morphology and structure characterization of Pd_3Pb square nanoplates. a,b) TEM, c) HRTEM, d) SAED, e) TEM-EDX elemental mapping, f) TEM-EDX spectrum, and g) XPS analysis of Pd 3d in commercial Pd/C and Pd_3Pb square nanoplates. h) AFM image and i) the corresponding height profiles of Pd_3Pb square nanoplates.

and enclosed by (100) facets. The compositional ratio of Pd to Pb in Pd_3Pb square nanoplates is determined to be ≈3/1 by EDX analysis (Figure 1e and Figure S1, Supporting Information), being in accordance with the results of inductively coupled plasma atomic emission spectroscopy (ICP-AES) and XPS. TEM-EDX line scan (Figure 1g) and point scan (Figure S2, Supporting Information) of the Pd_3Pb square nanoplates reveal that Pd and Pb distribute uniformly in the center and the edge of nanoplates (NP).

XPS spectra were used to analyze valence state of Pd for commmercial Pd/C and Pd_3Pb SNP. All the binding energies were calibrated to C 1s adventitious carbon at 284.8 eV to eliminate differences in sample charging. The core level XPS spectra of Pd 3d (Figure 1g) show that the majority of surface Pd in Pd_3Pb SNP is in metallic state, while nearly half of that in commercial Pd/C catalyst is in oxidized state of PdO (Figure S3, Supporting Information). For Pd_3Pb SNP, a portion of surface Pb atoms are in oxidized state of PbO (Figure S4, Supporting Information), which could prevent Pd atoms from being oxidized. Most importantly, Pd $3d_{5/2}$ and Pd $3d_{3/2}$ peaks of Pd_3Pb SNP were centered at 340.7 and 335.4 eV, respectively, shifting to higher binding energy with respect to those for Pd single metal at 340.1 and 335.1 eV.[10] This positive shifting in the d-band center of the intermetallic Pd_3Pb SNP is due to the d–d band hybridization occurring between Pd and Pb, indicating that the density of states (DOS) at the Fermi level decreases by filling the Pd d-band. It is widely accepted that a positive core-level XPS peak shift of Pd can weaken the interaction between Pd and the reactant or intermediate due to a downshift of the d-band center, resulting a weaker oxygen or CH_3OH binding energy that would enhance the catalytic activity significantly.[11] AFM was further used to evaluate the thickness of Pd_3Pb square nanoplates. The cross-section and height profile (Figure 1h,i) analysis reveal that the thickness of Pd_3Pb square nanoplates is ≈5.2 nm and thus the Pd_3Pb square nanoplates exhibit the relatively high surface area-to-volume ratio and high density of exposed atoms on their surface, which would enhance the catalytic performance significantly.[12]

The synthesis of thin 2D Pd-based bimetallic NS and NP without the use of carbon monoxide (CO) as a strong capping agent has long been a big challenge since metal atoms prefer to connect in 3D and form a close-packed structure.[13] Totally different from the previous synthetic strategy for 2D Pd nanosheets, herein we found that the molar ratio of Pd to Pb and the moderate amount of NH_4Br during the synthesis are the key factors in making Pd_3Pb SNP (Figure S5, Supporting Information). The content of $Pb(acac)_2$ used for the synthesis of Pd_3Pb square nanoplates is far beyond the stoichiometric ratio of 3/1. Without the use of $Pb(acac)_2$, only small Pd nanoparticles were obtained (Figure S6, Supporting Information). When the content of $Pb(acac)_2$ were changed from 32 mg (for Pd_3Pb square nanoplates) to 24, 16, 8, and 4 mg, the morphologies of Pd_3Pb changed from square nanoplates to NPA (named as NPA-4, NPA-3, NPA-2, and NPA-1, respectively) (Figure S7, Supporting Information). **Figure 2**a,b shows the representative TEM and HRTEM image of Pd_3Pb NPA-3. The HRTEM image (Figure 2b) shows that Pd_3Pb NPA-3 is highly crystalline and enclosed by (111) facets, different from the Pd_3Pb SNP enclosed by (100) facets. It should be noted the composition ratio of Pd to Pb is always kept at

≈3/1 for Pd_3Pb square nanoplates and nanoplate assemblies, confirmed by the EDX results (Figure 2c,d and Figure S8, Supporting Information).

Herein, NH_4Br is indispensable in forming Pd_3Pb square nanoplates due to the strong selective bonding of Br^- on (100) of *fcc* Pd_3Pb.[10a] Without NH_4Br, only small dendrites were made (Figure S9, Supporting Information). Also, the ratio of oleylamine to 1-octadecene plays an important role in making high-quality Pd_3Pb square nanoplates (Figure S10, Supporting Information). Without the existence of oleylamine, we cannot obtain any products. Meanwhile, the amount of AA is also important in the formation of the Pd_3Pb square nanoplates (Figure S11, Supporting Information). With half amount of AA used and keeping other parameters unchanged, the size of Pd_3Pb square nanoplates became inhomogeneous, while twice the amount of AA induced the formation of the Pd_3Pb NPA instead of the Pd_3Pb square nanoplates.

The powder X-ray diffraction (PXRD) technique is further used to analyze the crystalline structure of the as-synthesized Pd_3Pb square nanoplates and nanoplate assemblies (Figure 2e). All the samples are highly crystalline with ordered intermetallic Pd_3Pb phase [Joint Committee on Powder Diffraction Standards No. 50-1631], being in accordance with the Pd_3Pb intermetallic phase reported by DiSalvo and co-workers.[8b,14] It is interesting to find that the relative intensity ratios of $I_{(100)}/I_{(111)}$ and $I_{(200)}/I_{(111)}$ increase apparently with increasing the $Pb(acac)_2$ content (Figure 2f), reflecting the abundance of (100) facets of Pd_3Pb SNP, which is in accordance with the HRTEM results.[15]

To evaluate the catalytic performance of Pd_3Pb SNP and NPA with tunable crystalline orientation, they were first deposited on carbon support and then washed with ethanol and acetic acid mixture to remove the surfactant.[16] Carbon-supported catalysts (Figure S12, Supporting Information) were sonicated as homogeneous ink and further deposited on glassy carbon rotating disk electrode (GC-RDE). **Figure 3**a shows the ORR polarization curves of Pd_3Pb SNP, Pd_3Pb NPA with different crystalline orientation, Pd/C and Pt/C in O_2-saturated 0.1 M KOH solution with a rotation rate of 1600 rpm, and a sweep rate of 10 mV s^{-1}. The 2D Pd_3Pb nanostructures show crystalline orientation-dependent electrocatalytic activity for ORR (Figure 3a,b). Figure 3b,c shows the mass activities of Pd_3Pb SNP and NPA increase accordingly with the PXRD intensity ratio of $I_{(200)}/I_{(111)}$ increase, indicating that the mass activity is closely related to the facet orientation of Pd_3Pb nanocrystals. The Pd_3Pb square nanoplates with (100) preferred orientation show higher ORR catalytic activity than that of Pd_3Pb nanoplates assemblies with orientation of (111) facets. The above results indicate that (100) facets are the dominating active site for ORR on intermetallic 2D Pd_3Pb nanoplates. The half-wave potential of Pd_3Pb SNP is 0.887 V, 43 mV more positive than that of the commercial Pt/C, indicating much enhanced electrocatalytic activity of Pd_3Pb SNP for ORR. The mass activity of Pd_3Pb SNP is 0.78 A mg^{-1} Pd at 0.9 V, 7.1 times higher than that of commercial Pt/C (0.11 A mg^{-1} Pt) and 13 times higher than that of commercial Pd/C (0.06 A mg^{-1} Pd) (Figure 3b). To the best of our knowledge, the present Pd_3Pb SNP is better than all the state-of-art Pd-based catalysts reported to date for ORR in alkaline media (Table S1, Supporting Information).
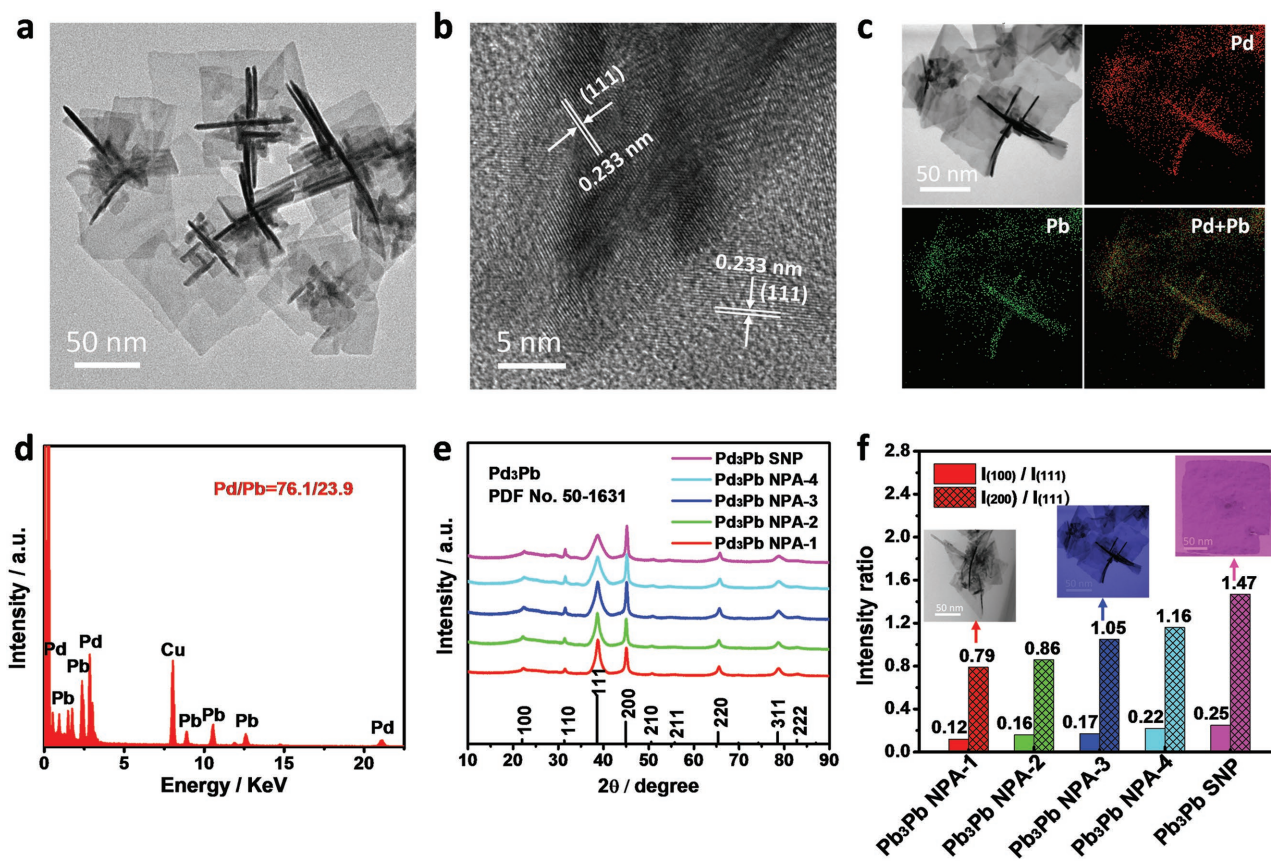
Figure 2. Morphology and structure characterization of Pd$_3$Pb NPA-3. a) Representative TEM image, b) HRTEM, c) TEM-EDX elemental mapping, and d) TEM-EDX spectrum. e) PXRD patterns of Pd$_3$Pb nanoplates assemblies and Pd$_3$Pb square nanoplates. f) The PXRD intensity ratio of $I_{(100)}/I_{(111)}$ and $I_{(200)}/I_{(111)}$. The inset of (f) shows the corresponding TEM image.

The enhanced ORR catalytic activity of Pd$_3$Pb SNP could be attributed to its positive core-level XPS peak shift of Pd that can weaken the interaction between Pd and the reactant or intermediate due to a downshift of the d-band center, resulting a weaker oxygen binding energy that would enhance the catalytic activity significantly.[11] To understand the reaction pathway of Pd$_3$Pb square nanoplates for ORR, the kinetics was investigated by rotating disk electrode from 400 to 2025 rpm, and the kinetic parameters were calculated by using the Koutecky–Levich equation (Figure 3d).[17] The number of transferred electrons was calculated to be ≈4 at various potentials from 0.6 to 0.8 V, indicating that Pd$_3$Pb SNP favors a 4 e$^-$ oxygen reduction process.[17b,18]

The electrochemical ADT of the Pd$_3$Pb SNP was evaluated at the potential between 0.6 and 1.0 V versus RHE in 0.1 M KOH solution. The ORR polarization curves of Pd$_3$Pb SNP before and after 1000 and 5000 potential cycles are shown in Figure 3e. After 5000 cycles, the half-wave potential of ORR polarization curves degrades by only 10 mV, and the mass activity remains 73.3% of the initial cycle for Pd$_3$Pb square nanoplates (Figure 3f), much better than that of commercial Pt/C with a degradation of 53 mV for half-wave potential and only 36.3% of its original mass activity, and better than that of commercial Pd/C with a degradation of 17 mV for half-wave potential and only 70.0% of its original mass activity (Figure S13, Supporting

Information). The structure of carbon-supported Pd$_3$Pb SNP after the durability test was characterized by TEM, TEM-EDX elemental mappings, showing that there was negligible change on the morphology and composition of Pd$_3$Pb SNP after the long-term cycles (Figure S14, Supporting Information). The ordered intermetallic structure of Pd$_3$Pb SNP, providing strong interaction between Pb and Pd to avoid deactivation of catalyst during the ORR progress, contributes to their long-term ORR catalytic stability.[8]

The methanol tolerance performance of Pd-based catalysts for ORR is obbligato since methanol would crossover from anode to cathode through the proton exchange membranes, which poison the electrocatalysts at the cathode and reduce the open-circuit potential.[8b,19] The ORR polarization curves of the Pd$_3$Pb square nanoplates was examined in O$_2$-saturated 0.1 M KOH containing 0.5 M CH$_3$OH (**Figure 4**a). The Pd$_3$Pb square nanoplates are highly methanol-tolerant in the presence of 0.5 M methanol by showing no methanol oxidation peak. However, under the same condition, the commercial Pt/C catalyst shows significant methanol oxidation peak at 0.84 V, while the commercial Pd/C exhibits a weaker methanol oxidation peak at 0.8 V. Moreover, we also performed ADT of the Pd$_3$Pb square nanoplates at the potential between 0.6 and 1.0 V versus RHE in 0.1 M KOH + 0.5 M CH$_3$OH solution. As shown in Figure 4b, the half-wave potential of the Pd$_3$Pb SNP degrade by only
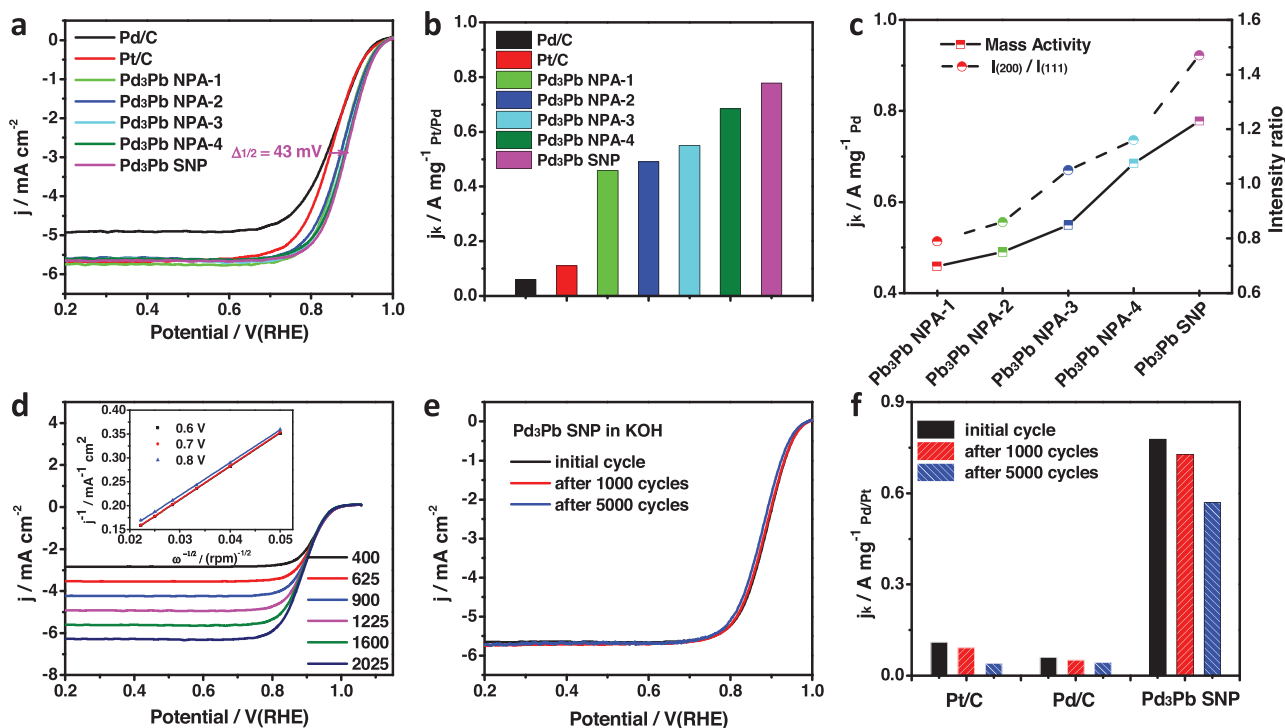
Figure 3. Electrocatalytic performance of Pd_3Pb SNP, Pd_3Pb NPA, Pd/C, and Pt/C for ORR. a) ORR polarization curves, b) mass activities at 0.9 V versus RHE, c) relationship between mass activities and the PXRD intensity ratio of $I_{(200)}$ to $I_{(111)}$, d) Rotating-disk voltammograms of Pd_3Pb SNP in O_2-saturated 0.1 M KOH at different rotation rates with a sweep rate of 10 mV s^{-1}. The inset of (d) shows the corresponding Koutecky–Levich plots. e) ORR polarization curves of Pd_3Pb SNP catalyst in O_2-saturated 0.1 M KOH before and after different potential cycles between 0.6 and 1.0 V versus RHE. f) The changes on mass activities of Pd_3Pb SNP, Pd/C, and Pt/C catalyst before and after different potential cycles.

13 mV, and its mass activity remains 77% even after 5000 cycles (Figure 4c), indicating the Pd_3Pb square nanoplates exhibit excellent stability even in the presence of 0.5 M CH_3OH.

To unravel the excellent methanol tolerance on the Pd_3Pb SNP, we performed DFT calculations. The adsorption energy of methanol on Pd_3Pb, Pd (111), and Pt (111) is calculated, with optimized adsorption geometries (Figure 4d and Figure S15, Supporting Information). The results reveal that presence of Pb decreases adsorption strength of methanol and the calculated $E_{methanol}$ follows the order of Pd_3Pb (100) < Pd (111) < Pt (111), with Pd_3Pb (100) having the lowest adsorption energy. Density of states of Pd_3Pb, Pd, and Pt are shown in Figure 4e. The 3d states of Pd_3Pb closest to Fermi level shift far away compared with those of Pd and Pt. The corresponding d-band center of Pd_3Pb, Pd, and Pt is calculated as −0.89, −0.84, and −0.40 eV with the d-band center of Pd_3Pb being the lowest. Differential charge density of Pd_3Pb (100) model (Figure 4f) reveals that charge is transferred from Pb atoms to Pd atoms, derived from the higher electronic affinity of Pd. Being in accordance with electrochemically measured results that (100) dominated Pd_3Pb SNP exhibits the best methanol tolerance performance, the charge transfer induced by lower shift of the d-band center on (100) dominated Pd_3Pb nanoplates is the key for boosting methanol-tolerance ORR performance.

To summarize, we demonstrate the first example in the controlled synthesis of a new class of intermetallic Pd_3Pb square nanoplates and nanoplates assemblies for boosting ORR with excellent methanol tolerance behavior. We found

that the crystalline orientation in as-made 2D Pd_3Pb nanostructure plays the key role in tuning ORR catalysis, in which Pd_3Pb SNP with (100) facet orientation is most active. The intermetallic Pd_3Pb SNP shows much higher activity and stability for ORR than commercial Pt/C catalyst in alkaline electrolyte. In particular, we found that the Pd_3Pb SNP shows much higher methanol tolerance behavior compared to that of commercial Pt/C and Pd/C during ORR catalysis. DFT calculations reveal that Pd_3Pb has the 3d states of closer to Fermi level than Pd and Pt, and Pd_3Pb SNP with (100) preferred orientation has the lowest methanol adsorption energy, which is the key factor in enhancing its methanol-tolerance performance. This study opens a new way for tuning the crystalline orientation of 2D Pd_3Pb nanostructures in boosting ORR with high methanol tolerance as highly efficient non-Pt ORR catalysts.

Experimental Section

Chemicals: Palladium acetylacetonate ($Pd(acac)_2$, 97%), lead(II) acetylacetonate ($Pb(acac)_2$, 99%), oleylamine (OAm, >70%), and ODE (technical grade, 90%) were obtained from Sigma-Aldrich. Ammonium bromide (NH_4Br) was purchased from Xilong Chemical Factory Co, Ltd. L-AA (reagent grade, 99%) and isopropanol were obtained from J&K Scientific. Potassium hydroxide (KOH), ethanol, methanol, and cyclohexane were supplied by Beijing Tongguang Fine Chemicals Company. Commercial Pt/C catalyst (20 wt%) was obtained from Johnson-Matthey Corporation and commercial Pd/C catalyst (10 wt%)
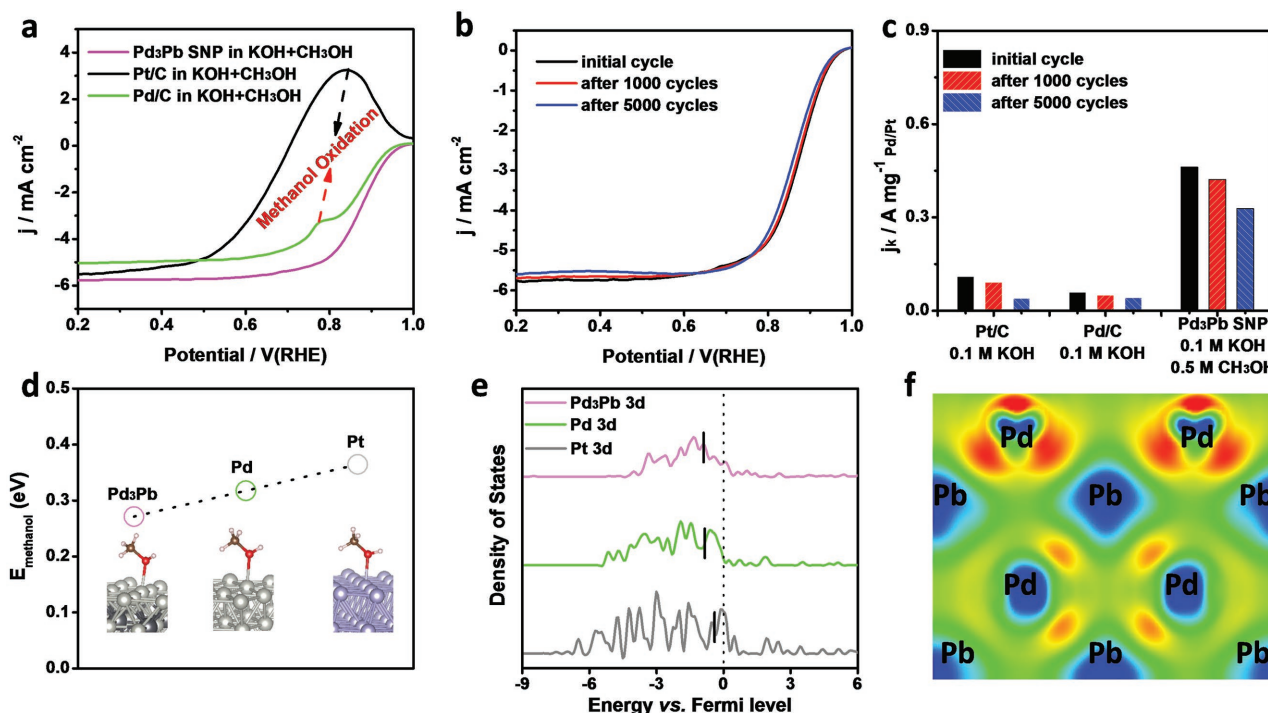
ADVANCED
SCIENCE NEWS
www.advancedsciencenews.com

small
methods
www.small-methods.com

Figure 4. a) ORR polarization curves of Pd$_3$Pb SNP, Pd/C, and Pt/C in O$_2$-saturated 0.1 M KOH + 0.5 M CH$_3$OH. b) ORR polarization curves of Pd$_3$Pb SNP in O$_2$-saturated 0.1 M KOH+ 0.5 M CH$_3$OH before and after different potential cycles between 0.6 and 1.0 V versus RHE. c) Changes on mass activities. d) Trend in adsorption energy of methanol over Pd$_3$Pb (100), Pd (111), and Pt (111). e) Density of States of Pd$_3$Pb, Pd, and Pt. The vertical line denotes d-band center of corresponding catalysts. f) Differential charge density of the side view of Pd$_3$Pb (100) surface model. The red/light (blue/dark) areas mark an increase (decrease) of the charge density.

was purchased from Sigma-Aldrich. Nafion (5%) was bought from Alfa Aesar. All the chemicals were used as received without further purification. All solutions were freshly prepared with ultrapure water (18.2 MΩ cm^{-1}).

Synthesis of Pd$_3$Pb Square Nanoplates and Pd$_3$Pb Nanoplates Assemblies: In a typical preparation of Pd$_3$Pb SNP, palladium acetylacetonate (Pd(acac)$_2$, 7.6 mg), lead(II) acetylacetonate (Pb(acac)$_2$, 32 mg), L-ascorbic acid (35.6 mg), ammonium bromide (25 mg), 2.5 mL oleylamine, and 2.5 mL 1-octadecene were added into a 25 mL vial (Synthware). After the vial had been capped, the mixture was ultrasonicated for around 60 min to get a homogeneous mixture, then heated from room temperature to 100 °C in 25 min and kept at 100 °C for 120 min in an oil bath. After being cooled to room temperature, the black colloidal product was collected by centrifugation at 6500 rpm and washed three times with cyclohexane. For the synthesis of Pd$_3$Pb nanoplates assemblies, all the conditions are similar to those of Pd$_3$Pb single nanoplates except changing the amount of lead(II) acetylacetonate from 32 to 24 mg, 16, 8, and 4 mg, respectively (denoted as NPA-4, NPA-3, NPA-2, and NPA-1). All the synthesized samples were dispersed in 20 mL cyclohexane for further use.

Characterization: TEM images were taken from a Tecani-G2 T20 operated at 200 kV. HRTEM, SAED, and EDX were carried out on a JEOL 2100F TEM (200 kV). Power X-ray diffraction (PXRD) patterns were collected using a PANalytical powder diffractometer equipped with a Cu radiation source (λ = 0.15406 nm). The concentration of catalysts was determined by ICP-AES on a Prodigy. XPS tests were carried out with Thermo Scientific Escalab 250Xi *XPS tests were carried out with Thermo Scientific Escalab 250Xi* using a monochromated Al-K_α (1486.5 eV) X-ray radiation. The emitted photoelectrons were detected using a hemispherical analyzer at a pass energy of 100 eV for full spectrum and 20 eV for high resolution XPS peak. All the binding

energies were calibrated to C 1s adventitious carbon at 284.8 eV to eliminate differences in sample charging and the XPS spectra were fitted by XPSPEAK41. AFM analysis was performed using Asylum Research, MFP-3D-BIO.

Electrochemical Measurements: The as-prepared Pd$_3$Pb square nanoplates and Pd$_3$Pb nanoplates assemblies were loaded on carbon before the electrochemical tests. Typically, the as-prepared Pd$_3$Pb dispersed in 20 mL of cyclohexane, Ketjen Black-300J carbon (6 mg) dispersed in 10 mL of ethanol and 50 mL of cyclohexane were mixed and then sonicated for 1 h. The products were collected by centrifugation and then redispersed in 10 mL of ethanol and 1 mL of acetic acid mixture. After being sonicating for 30 min, the products were collected by centrifugation and further washed with ethanol for two times. Then, the products were dried under 60 °C for 2 h to obtain the final catalysts. The catalysts were redispersed in the mixture containing isopropanol, H$_2$O, and Nafion (5%) (v:v:v = 1:1:0.01) to form a homogeneous catalyst ink by sonicating for 60 min. The concentration of Pd was controlled to be 0.12 mg$_{Pd}$ mL^{-1} based on ICP-AES measurement. 10 μL of the dispersion was dropped onto the GC electrode (5 mm, 0.196 cm^2) to obtain the working electrodes with the loading amount of Pd at 6.1 μg cm^{-2}.

Electrochemical experiments were performed with a CHI 760e Electrochemical Workstation (Shanghai Chenhua Instrument Corporation, China) in a conventional three-electrode cell, where a RDE (Pine Instruments, area: 0.196 cm^2), saturated calomel electrode, and Pt foil (1 cm × 1 cm) were used as the working, reference and counter electrodes, respectively. ORR measurements were conducted in a 0.1 M KOH solution purged with saturated oxygen during the measurement. The scan and rotation rates for ORR measurement were 10 mV s^{-1} and 1600 rpm. The electrochemical ADT were performed at room temperature in O$_2$-saturated 0.1 M KOH solutions by applying the cyclic

potential sweeps between 0.6 and 1.0 V versus RHE. All electrochemical experiments were performed at room temperature.

The kinetic current (j_k) can be calculated by using the Koutecky–Levich equation

$$\frac{1}{j} = \frac{1}{j_k} + \frac{1}{j_d} = \frac{1}{j_k} + \frac{1}{B\omega^{1/2}} \qquad (1)$$

$$B = 0.2nF\left(D_{O_2}\right)^{2/3} \nu^{-1/6} C_{O_2} \qquad (2)$$

where j is the measured current, j_d is the diffusion limited current, n is the number of electrons transferred, F is Faraday's constant ($F = 96\ 485$ C mol^{-1}), D_{O_2} is the diffusion coefficient of O_2 in 0.1 M KOH ($D_{O_2} = 1.9 \times 10^{-5}$ cm^2 s^{-1}), ν is the kinematic viscosity of the electrolyte ($\nu = 0.01$ cm^2 s^{-1}), ω is the angular frequency of rotation, and C_{O_2} is the concentration of molecular oxygen in 0.1 M KOH solution ($C_{O_2} = 1.2 \times 10^{-6}$ mol cm^{-3}).[17a]

Calculation Method: The DFT calculations were carried out using the Vienna ab initio simulation package with the projector augmented wave[20] pseudopotentials and the function of Perdew, Burke, and Ernzerhof[21] based on the generalized gradient approximation. A cut-off energy of 400 eV was used for the plane-wave basis set. The Brillouin zone was sampled on the basis of the Monkhorst–Pack scheme with a $3 \times 3 \times 1$ k-point mesh.[22] The convergence criteria of self-consistent field for electronic relaxation and force for atomic relaxation were 1×10^{-5} eV and 0.02 eV Å^{-1}, respectively. The methanol adsorption energy $E_{methanol}$ was defined as $E_{methanol} = E_{sub+methanol} - E_{sub} - E_{iso}$, where $E_{sub+methanol}$, E_{sub} and E_{iso} were the total energies of catalyst substrates with the methanol adsorbate, clean substrates, and isolated methanol molecule, respectively. For d-band center calculation, the interval from -1 to 0 eV versus Fermi level was taken into account, for precisely weighing the contribution made by the states closest to Fermi level. Spin polarization were considered in all the calculations.

Supporting Information

Supporting Information is available from the Wiley Online Library or from the author.

Conflict of Interest

The authors declare no conflict of interest.

[1] a) A. Chen, C. Ostrom, *Chem. Rev.* **2015**, *115*, 11999; b) V. R. Stamenkovic, B. Fowler, B. S. Mun, G. Wang, P. N. Ross, C. A. Lucas, N. M. Marković, *Science* **2007**, *315*, 493; c) B. C. Steele, A. Heinzel, *Nature* **2001**, *414*, 345; d) W. Wang, F. Lv, B. Lei, S. Wan, M. Luo, S. Guo, *Adv. Mater.* **2016**, *28*, 10117; e) M. Shao, Q. Chang, J.-P. Dodelet, R. Chenitz, *Chem. Rev.* **2016**, *116*, 3594.

[2] a) L.-L. Shen, G.-R. Zhang, S. Miao, J. Liu, B.-Q. Xu, *ACS Catal.* **2016**, *6*, 1680; b) Y. Bing, H. Liu, L. Zhang, D. Ghosh, J. Zhang, *Chem. Soc. Rev.* **2010**, *39*, 2184; c) K. J. Mayrhofer, M. Arenz, *Nat. Chem.* **2009**, *1*, 518.

[3] a) S. Sun, C. B. Murray, D. Weller, L. Folks, A. Moser, *Science* **2000**, *287*, 1989; b) D. Li, C. Wang, D. S. Strmcnik, D. V. Tripkovic, X. Sun, Y. Kang, M. Chi, J. D. Snyder, D. van der Vliet, Y. Tsai, *Energy Environ. Sci.* **2014**, *7*, 4061.

[4] H. A. Gasteiger, S. S. Kocha, B. Sompalli, F. T. Wagner, *Appl. Catal., B* **2005**, *56*, 9.

[5] a) Z. Xia, L. An, P. Chen, D. Xia, *Adv. Energy Mater.* **2016**, *6*, 1600458; b) H. Yin, H. Tang, D. Wang, Y. Gao, Z. Tang, *ACS Nano* **2012**, *6*, 8288.

[6] a) Y. Yan, J. S. Du, K. D. Gilroy, D. Yang, Y. Xia, H. Zhang, *Adv. Mater.* **2017**, *29*, 1605997; b) U. Din, M. Aizaz, F. Saleem, B. Ni, Y. Yong, X. Wang, *Adv. Mater.* **2017**, *29*, 1604994; c) M. Liu, Y. Lu, W. Chen, *Adv. Funct. Mater.* **2013**, *23*, 1289; d) C. Bianchini, P. K. Shen, *Chem. Rev.* **2009**, *109*, 4183.

[7] a) M. Luo, Y. Sun, L. Wang, S. Guo, *Adv. Energy Mater.* **2017**, *7*, 1602073; b) N. N. Cheng, Z. Starkewolf, R. A. Davidson, A. Sharmah, C. Lee, J. Lien, T. Guo, *J. Am. Chem. Soc.* **2012**, *134*, 1950.

[8] a) M. Wencka, M. Hahne, A. Kocjan, P. Koželj, D. Korže, Z. Jagličić, M. Sorić, P. Popčević, J. Ivkov, *Intermetallics* **2014**, *55*, 56; b) Z. Cui, H. Chen, M. Zhao, F. J. DiSalvo, *Nano Lett.* **2016**, *16*, 2560; c) G. Jiang, H. Zhu, X. Zhang, B. Shen, L. Wu, S. Zhang, G. Lu, Z. Wu, S. Sun, *ACS Nano* **2015**, *9*, 11014; d) M. Armbrüster, G. Wowsnick, M. Friedrich, M. Heggen, R. Cardoso-Gil, *J. Am. Chem. Soc.* **2011**, *133*, 9112.

[9] a) D. Deng, K. Novoselov, Q. Fu, N. Zheng, Z. Tian, X. Bao, *Nat. Nanotechnol.* **2016**, *11*, 218; b) T. Ling, J. J. Wang, H. Zhang, S. T. Song, Y. Z. Zhou, J. Zhao, X. W. Du, *Adv. Mater.* **2015**, *27*, 5396; c) H. Liao, J. Zhu, Y. Hou, *Nanoscale* **2014**, *6*, 1049.

[10] a) X. Huang, S. Tang, X. Mu, Y. Dai, G. Chen, Z. Zhou, F. Ruan, Z. Yang, N. Zheng, *Nat. Nanotechnol.* **2011**, *6*, 28; b) A. Tressaud, S. Khairoun, H. Touhara, N. Watanabe, *Z. Anorg. Allg. Chem.* **1986**, *540*, 291.

[11] a) K. Lee, O. Savadogo, A. Ishihara, S. Mitsushima, N. Kamiya, K.-I. Ota, *J. Electrochem. Soc.* **2006**, *153*, A20; b) M. Wakisaka, S. Mitsui, Y. Hirose, K. Kawashima, H. Uchida, M. Watanabe, *J. Phys. Chem. B* **2006**, *110*, 23489.

[12] N. Yang, Z. Zhang, B. Chen, Y. Huang, J. Chen, Z. Lai, Y. Chen, M. Sindoro, A. L. Wang, H. Cheng, *Adv. Mater.* **2017**, *29*, 1700769.

[13] a) W.-C. Cheong, C. Liu, M. Jiang, H. Duan, D. Wang, C. Chen, Y. Li, *Nano Res.* **2016**, *9*, 2244; b) X. Qiu, H. Zhang, P. Wu, F. Zhang, S. Wei, D. Sun, L. Xu, Y. Tang, *Adv. Funct. Mater.* **2017**, *27*, 1603852; c) Y. Li, Y. Yan, Y. Li, H. Zhang, D. Li, D. Yang, *CrystEngComm* **2015**, *17*, 1833; d) A. Mahmood, H. Lin, N. Xie, X. Wang, *Chem. Mater.* **2017**, *29*, 6329; e) F. Saleem, Z. Zhang, B. Xu, X. Xu, P. He, X. Wang, *J. Am. Chem. Soc.* **2013**, *135*, 18304.

[14] T. Gunji, S. H. Noh, T. Tanabe, B. Han, C. Y. Nien, T. Ohsaka, F. Matsumoto, *Chem. Mater.* **2017**, *29*, 2906.

[15] a) W. Niu, Y. Gao, W. Zhang, N. Yan, X. Lu, *Angew. Chem.* **2015**, *127*, 8389; b) Y. Jiang, Y. Yan, W. Chen, Y. Khan, J. Wu, H. Zhang, D. Yang, *Chem. Commun.* **2016**, *52*, 14204.

[16] L. Bu, N. Zhang, S. Guo, X. Zhang, J. Li, J. Yao, T. Wu, G. Lu, J.-Y. Ma, D. Su, *Science* **2016**, *354*, 1410.

[17] a) S. Guo, S. Zhang, L. Wu, S. Sun, *Angew. Chem.* **2012**, *124*, 11940; b) S. Kondo, M. Nakamura, N. Maki, N. Hoshi, *J. Phys. Chem. C* **2009**, *113*, 12625.

[18] a) J. Yang, J. Hu, M. Weng, R. Tan, L. Tian, J. Yang, J. Amine, J. Zheng, H. Chen, F. Pan, *ACS Appl. Mater. Interfaces* **2017**, *9*, 4587;

b) H. Tabassum, R. Zou, A. Mahmood, Z. Liang, S. Guo, *J. Mater. Chem. A* **2016**, *4*, 16469.

[19] W. Wang, Q. Huang, J. Liu, Z. Zou, Z. Li, H. Yang, *Electrochem. Commun.* **2008**, *10*, 1396.

[20] P. E. Blöchl, *Phys. Rev. B* **1994**, *50*, 17953.

[21] J. P. Perdew, K. Burke, M. Ernzerhof, *Phys. Rev. Lett.* **1996**, *77*, 3865.

[22] H. J. Monkhorst, J. D. Pack, *Phys. Rev. B* **1976**, *13*, 5188.